High-Throughput Packed-Bed Microreactors with In-Line Analytics for the Discovery of Asphaltene Deposition Mechanisms

Chuntian Hu and Ryan L. Hartman
Dept. of Chemical and Biological Engineering, The University of Alabama, Tuscaloosa, AL 35487

DOI 10.1002/aic.14542
Published online July 10, 2014 in Wiley Online Library (wileyonlinelibrary.com)

Understanding asphaltene nanoaggregation kinetics is a key to predicting the deposition in pure quartz-grain porous media. High-throughput quartz packed-bed microreactors (μPBRs) were, therefore, designed to provide mechanistic insights by merging oilfield chemistry and microchemical systems. In-line UV-Vis spectroscopy and pressure transducer were used to characterize the stable packing of quartz particles with porosity of ~40% and permeability of $\sim 5.5 \times 10^{-13}$ m^2. *Temperature (25.0–90.0°C),* n-*heptane composition (50.0–80.0 vol %), and* n-*alkane (*n-C_5 *to* n-C_9*) were all observed to influence asphaltenes deposition in the porous media, and reduced dispersion was obtained in the damaged packed-bed by estimating dispersion coefficients and the Bodenstein number. Deposition by mechanical entrapment dominated the mechanism in all scenarios, as discovered by the simplified Kozeny–Carman and Civan's permeability-porosity relationships. The results could aid in the design of remediations that minimize production losses of considerable economic magnitude.* © 2014 American Institute of Chemical Engineers *AIChE J*, 60: 3534–3546, 2014
Keywords: asphaltenes, deposition, precipitation, packed-bed microreactor, residence time distribution

Introduction

Asphaltene science broadly impacts chemicals manufacturing, transportation, roofing, and energy production. Every barrel of crude oil produced upstream is comprised of natural gas, hydrocarbon, and aqueous phases. The potential for thermodynamic instabilities of asphaltenes within hydrocarbon phases necessitates understanding asphaltene accumulation mechanisms: a global problem in upstream conventional and unconventional energy production that also influences downstream chemicals refining. Asphaltene science in general is important to green chemistry and sustainability. Tremendous potential exists for lab-on-chip devices to make significant contributions across broad fields of science where molecular, nanoscale, and microscale understandings of asphaltene science are needed.

The precipitation and the resultant deposition of crude oil asphaltenes (i.e., asphaltene instability) are complex and problematic during oil production, transportation, and refining operations.[1–12] Due to their complexity, asphaltenes are defined by the solubility characteristics and not by a specific chemical compound. In the laboratory, asphaltenes are often defined as the *n*-heptane (or *n*-pentane) insoluble, toluene soluble components of a given crude oil. This definition of asphaltenes captures the most aromatic and polar components of a given crude oil, a broad molecular fingerprint, which challenges the determination of some fundamental asphaltenes parameters, such as molecular weight and solution behavior. The chemical composition, molecular structure, and other intrinsic properties vary with reservoir geography, pressure, temperature, and precipitant type.[1] Changes in reservoir pressure, temperature, and bulk fluid composition[13] are known to create asphaltene instability, and as a result their precipitation and deposition. Amidst such complex chemistry, universal science that connects the laboratory to production scenarios is highly sought after and for great reason.

Asphaltene precipitation and deposition can occur on any reservoir production surface, especially within the near-wellbore region where the pore volumes are confined and component concentrations achieve their maximum values.[14–16] The onset of precipitation occurs at the upper asphaltene precipitation pressure, and the rate achieves a maximum at the solvent bubble point.[15] Subsequent asphaltene deposition leads to the accumulation of organic material that constrains reservoir fluid flows. There are two widely accepted deposition models: adsorption and mechanical entrapment. In adsorption, asphaltene nanoparticles physically adsorb on porous media surfaces due to affinity, polarity, or other attractive forces. This process is reversible and its contribution to total mass deposited depends on the surface characteristics.[17] In mechanical entrapment, surface deposition, entrainment, and pore-throat plugging can all contribute to deposition.[15] Both deposition mechanisms reduce porosity and impair permeability, and in turn reservoir production rates effectively decline. Mechanical pigging and squeeze injection treatments are common operational techniques that

Additional Supporting Information may be found in the online version of this article.

Correspondence concerning this article should be addressed to R. L. Hartman at rhartman@eng.ua.edu.

remediate such damage. Mechanical pigging removes asphaltene deposits from the production casing downstream of the reservoir fluids exiting the porous media.[18] Squeeze injection treatments, on the other hand, target asphaltenes deposited within the porous reservoir matrix via chemical injection and shut-ins within the subterranean reservoir, and hence production is temporarily shutdown. Molecular, nanoscale, and microscale mechanistic insights are crucial for the accurate design of chemical remediation treatments that minimize the production losses during shut-ins while maximizing the production rates during the commencement of reservoir flow-backs.

Microchemical systems, characteristic of high surface-area-to-volume ratios and reduced heat- and mass-transfer resistances,[19–37] serve as ideal systems to investigate flow and reaction in porous media science scalable from the laboratory to production. Microreactors have made considerable advances in fine chemicals and pharmaceutical discovery and the rapid screening of catalysts. The choice of microreactor materials[19,30,38–45] depends on many factors, including the experimental conditions and ease of fabrication techniques. The advantages of silicon[19,42] and glass[41,43–45] microreactors are their capability of withstanding high pressures due to the bond strengths of the materials. *In situ* analyses of chemical transformations performed with transparent microreactors introduce further versatility and the potential for understanding multiphase systems. Transparent packed-bed microreactors (μPBRs) are well suited but to date have not been designed to investigate the deposition of asphaltenes. High-throughput chemical and physical information is readily available on demand by lab-on-chip designs that are capable of operating at high-pressures (>20 MPa) and temperatures (>350°C). The design of microsystems and their integration with online analytical techniques creates the potential to advance asphaltene science at characteristic length scales where computational techniques directly interface experimental laboratory techniques.

In the present study, two fields of science were merged, oilfield chemistry and microchemical systems, to investigate the deposition of asphaltenes in porous media. A transparent μPBR was designed in attempt to bridge the knowledge gap between molecular level events and oilfield production. For the first time, porosity losses and permeability impairments of μPBRs were studied, and as a result the dominant asphaltene deposition mechanism was revealed. The experimental results obtained in the present work could be useful in designing remediation treatments that minimize conventional and unconventional energy production losses of considerable economic magnitude.

Experimental

Materials and instruments

Ethanol (absolute), *n*-pentane (*n*-C_5, 98 mol %), *n*-hexane (*n*-C_6, HPLC grade), *n*-heptane (*n*-C_7, HPLC grade), *n*-octane (*n*-C_8, 98 mol %), and *n*-nonane (*n*-C_9, 99 mol %) were obtained from Alfa Aesar (Ward Hill, MA). Toluene and acetone (HPLC grade) were purchased from EMD (Millipore). BDH quartz sand (30–40 mesh) was acquired from VWR International (West Chester, PA). All liquids were used without further purification.

High-pressure syringe pumps (65DM) and PHD 2000 syringe pumps manufactured by Teledyne ISCO (Lincoln, NE) and Harvard Apparatus (Holliston, MA), respectively, were used in the present work. Check valves, pressure reducing valves, a microscale injector, and back pressure regulators were purchased from IDEX Heath & Science (Oak Harbor, WA). UV-Vis spectroscopy and pressure transducers were obtained from Ocean Optics (Dunedin, FL) and Honeywell Sensing & Control (Golden Valey, MN), respectively.

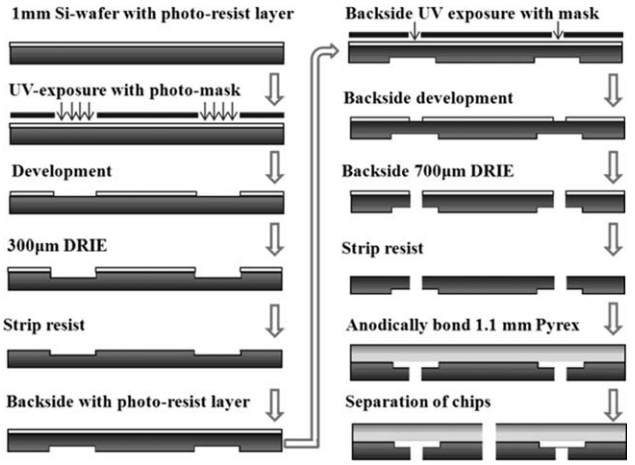

Figure 1. Schematic illustration of the fabrication process used to create μPBRs.

Preparation of asphaltenes and estimation of their solubility

The asphaltenes used in the present work were obtained from Wyoming crude oil deposit provided by Nalco Energy Services Headquarters. The crude oil deposit was dissolved in toluene, and the solution media was filtered by Whatman No. 1 filter paper in order to remove the insoluble organic and inorganic impurities. Next, *n*-heptane was injected and the dissolved asphaltenes precipitated. The precipitates were collected by Whatman No. 1 filter paper and oven-dried at 60°C for 24 h.

The solubility of the recovered asphaltenes in mixtures of pure toluene and *n*-alkanes at temperatures ranging from 25.0 to 90.0°C were estimated. Mixtures of *n*-alkanes and 4 g/L asphaltenes dissolved in toluene were maintained at constant temperatures for 24 h and then filtered using Whatman No. 3 filter paper. UV-Vis spectroscopy was used to measure the absorbance of asphaltenes in the filtrates. The precipitated asphaltenes in the filter paper were dried and the masses measured via analytical balance.

Fabrication of μPBRs. The transparent μPBRs were fabricated from a 1-mm polished single crystal silicon wafer and a 1.1-mm Pyrex wafer. Figure 1 schematically illustrates the fabrication process employed to create the microsystems, which primarily included (1) photolithography (spin-coating, exposure, and development), (2) deep reactive ion etching, (3) cleaning, (4) anodic bonding of the silicon wafer to the Pyrex wafer, and (5) dicing into chips. A photograph of the 45-μL μPBR with dimensions of 5.0 × 1.8 × 0.21 cm is shown in Figure 2a. The microchannel is 300 μm in depth and 9 mm in width. Near the exit, 30 rows of pillars of 20 μm in diameter are spaced 20 μm apart, as shown in Figure 2b. Figure 2c illustrates, each separately, the components of the μPBR system employed to study asphaltene accumulations.

Quartz particles were prepared from 30 to 40 mesh quartz sands by mortar and pestle in the presence of water. The smallest quartz particle fractions were collected using 500 and 635 mesh sieves. Ultrafine particles were removed by graduated cylinder introduced into an ultrasonic bath.

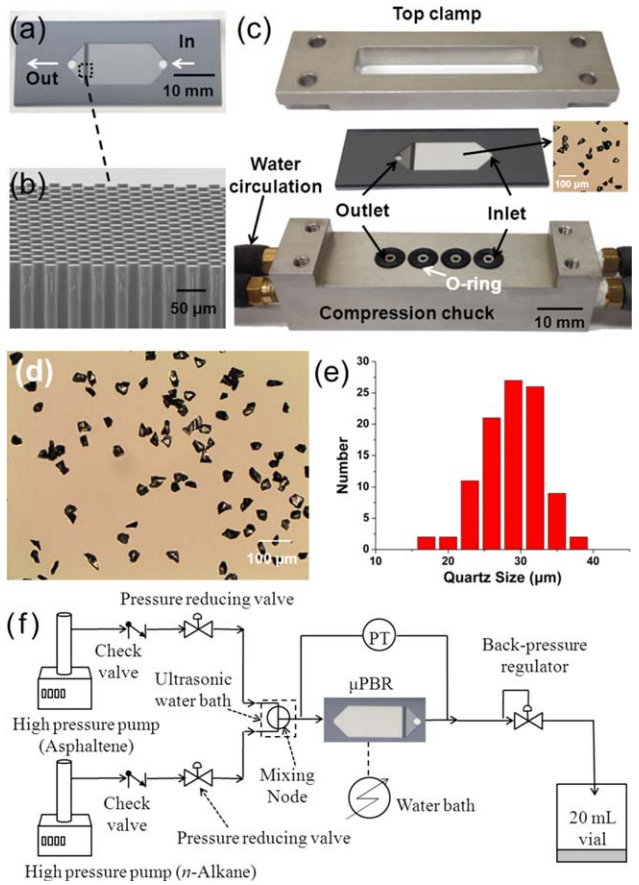

Figure 2. (a) Photograph of the μPBR. (b) SEM micrograph of pillars with diameter of 20 μm. (c) Separated components of the package system. (d) Microscope photograph and (e) the measured size distribution of quartz particles. (f) Schematic process flow diagram of the experimental setup used to study the deposition of asphaltenes in the μPBRs.

Microscope photographs of the recovered particles were obtained (see Figure 2d), and the size distributions were estimated by measurements of samples of 100 particles per micrograph image as shown in Figure 2e.

Asphaltene deposition apparatus

The process flow diagram engineered to study asphaltene accumulations in μPBRs is shown schematically in Figure 2f. Two high-pressure pumps were used to inject asphaltenes dissolved in toluene and *n*-alkanes into the μPBR at constant flow rates. Check valves ensured flow of fluids through the μPBR, whereas pressure relief devices (set to 689 kPa) were integrated to avoid the worst-case scenario of pumping into a closed system. The reagents in two laminar flow streams were combined in a stainless steel T-union placed in an ultrasonic bath to prevent plugging. In-line pressure transducers (689 kPa) enabled the monitoring of the pressure drop inside the μPBR. The packaged compression chuck system was connected to a water bath to control the temperature ranging from 25.0 to 90.0°C. At the outlet of the μPBR, a backpressure regulator maintained the outlet pressure of the microreactor at 35 kPa.

Residence time distribution measurements

Figure 3a illustrates the process flow diagram of the continuous in-line UV-Vis spectroscopy system designed to measure the residence time distributions (RTDs) of the μPBR. Carrier solvent (*n*-heptane) in 5-mL SGE glass syringes was delivered using a Harvard Apparatus PHD 2000 syringe pump at constant flow rates of 40.00 μL/min. A microscale injector (Figure 3b) was used to inject 1.0 μL of tracer (20 vol % acetone in *n*-heptane) in-line. Tracer dispersions were monitored in-line using UV-Vis spectroscopy at the outlet of the μPBR, where a flow cell with integrated 400-μm I.D. quartz capillary (Figure 3c) was connected. The microscale injector, packaged compression chuck, and the flow cell were interconnected using 0.005″ I.D. PFA tubing to reduce the dead volume. As before, a backpressure regulator maintained a constant pressure at the microreactor outlet of 35 kPa. Both deuterium and halogen lamps on the light source were allowed to warm up for at least 20 min before performing RTD experiments. Figure 3d shows the absorbance of acetone in *n*-heptane at concentrations ranging from 1.0 to 20.0 vol %. The peak absorbance wavelength, 277 nm, was chosen to maximize the signal-to-noise ratio and to improve the precision of the measurements, especially at low tracer absorbances.

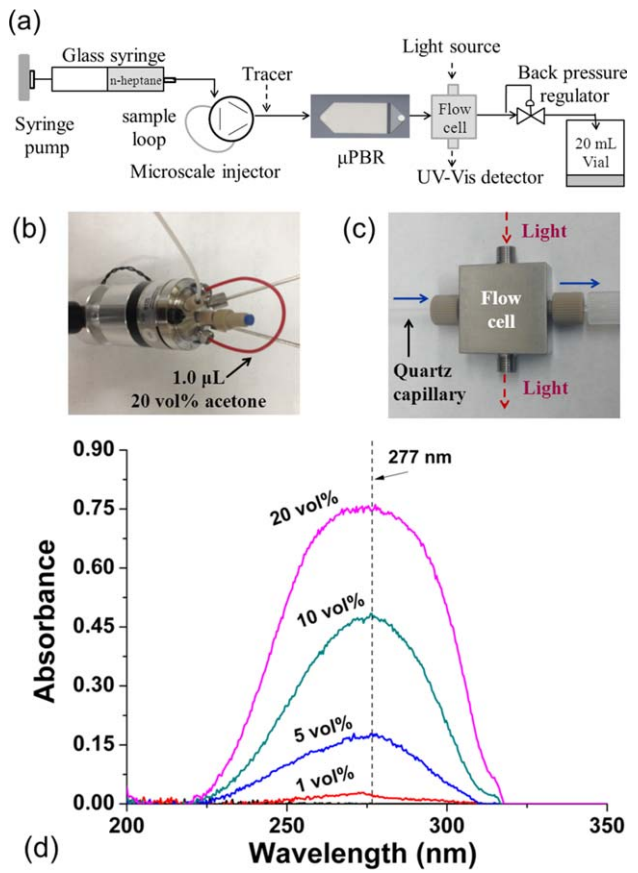

Figure 3. (a) Schematic process flow diagram of the continuous in-line UV-Vis spectroscopy used to measure RTDs. (b) Microscale injector with 1.0-μL sample loop (8 cm of 0.005″ I.D. tubing) and (c) flow cell with integrated 400-μm I.D. quartz capillary. (d) UV-Vis absorbance of acetone in *n*-heptane for different volume percentages.

Theoretical Approach

Characterization of porous media

Permeability and porosity are two important parameters that characterize porous media. Permeability is the ability of porous media to allow gas or liquid to pass through, whereas porosity is the amount of void space in a porous media. Two arbitrary porous media systems can have the same porosities but exhibit different permeability. Estimation of permeability is of pivotal importance for the description of hydrocarbon recovery.[46] Permeability κ (m^2) is commonly defined by Darcy's law, obtained empirically, as a proportionality coefficient in the relationship between flow rate Q (m^3/s) and pressure drop over a distance, expressed as[46,47]

$$\kappa = \frac{\mu Q}{A}\frac{L}{\Delta P} \tag{1}$$

where μ is the dynamic viscosity of the fluid (Pa · s), A the cross-sectional area normal to the direction of flow (m^2), ΔP the pressure drop across the porous media (Pa), and L is the axial length (m).

When precipitation occurs, for instance asphaltenes in hydrocarbon reservoirs, the extent of subterranean wellbore damage is commonly quantified by defining the dimensionless Skin Factor, which was originally considered by van Everdingen and Hurst.[48] The van Everdingen–Hurst Skin Factor, s, is defined as[17,49]

$$s = \Delta P \frac{2\pi\kappa_0 h}{Q\mu} \tag{2}$$

where h is the characteristic thickness of the production zone.

Porosity is given as the ratio of the volume of the void space, V_V, and total volume, V_T[50]

$$\varnothing = \frac{V_V}{V_T} \tag{3}$$

from which the actual fluid velocity u_i can be obtained by[51]

$$u_i = u/\varnothing \tag{4}$$

where u is the superficial velocity.

Tortuosity of porous media is defined as the ratio of the actual length to the straight length of a molecules flow path.[52,53] When the flow paths are not readily available, a previously recognized empirical tortuosity-porosity relationship, given by[53]

$$\mathcal{T}^2 = (a\varnothing^{1-m})^n \tag{5}$$

estimates the tortuosity, $\mathcal{T}$, where $a = 1$, $n = 1$, and $m = 2.14$ for unconsolidated sands systems.

Important parameters that characterize packed-beds include the length of the packed-bed, L, the superficial fluid velocity u, and the mean particle size d_P, from which the Reynolds number in a packed-bed, Re_P, can be determined[51]

$$Re_P = \frac{d_P u\,\rho}{(1-\varnothing)\mu} \tag{6}$$

In packed-bed systems, laminar conditions exist for $Re_P < 10$ and fully turbulent when $Re_P > 2000$. The hydraulic radius, r_H, is the cross-sectional, characteristic dimension of a cylindrical pore throat independent of a system's geometry defined by the boundary conditions. From the porosity, $\varnothing$, and the mean particle size, d_P, the hydraulic radius is estimated by[17]

$$r_H = \frac{\varnothing}{(1-\varnothing)}\frac{d_P}{6} \tag{7}$$

Dispersion model

In our previous work,[33] dispersion models for plug flow and open-open systems were used to accurately characterize single-phase and multiphase flows in microfluidics. The vessel dispersion number, D^*/uL, where D^* is the dispersion coefficient and L the microchannel length, approximates the degree of axial dispersion. For large deviations from plug flow, open–open boundary conditions have been shown to accurately describe dispersion within packed-beds when the dimensionless RTD, $E(\theta)$, is described by[54]

$$E(\theta) = \frac{1}{\sqrt{4\pi(D^*/uL)\theta}}\exp\left[-\frac{(1-\theta)^2}{4(D^*/uL)\theta}\right] \tag{8}$$

The maximum peak heights of $E(\theta)$ curves yield estimations of the vessel dispersion number, D^*/uL, and the axial dispersion coefficient, D^*. The ratio of convection to molecular diffusion, the Bodenstein number, Bo, defined as[54]

$$Bo = \frac{ud_E}{\mathcal{D}} \tag{9}$$

is estimated for known L/d_E ratios of 10^2 by combining[54]

$$\mathcal{D} = \frac{u^2 d_E^2}{192D^*} \tag{10}$$

into Eq. 9. Here, $\mathcal{D}$ is the molecular diffusivity, and d_E is the effective microchannel diameter of the rectangular μPBR.

Permeability-porosity relationships

It is generally understood that no universal permeability-porosity relationship describes all porous media. For packed columns, combining the Ergun equation with Darcy's Law for laminar flow yields[49,55–58]

$$\frac{\kappa}{\kappa_0} = \left(\frac{\varnothing}{\varnothing_0}\right)^3\left(\frac{1-\varnothing_0}{1-\varnothing}\right)^2 \tag{11}$$

which is also known as the simplified Kozeny–Carman equation. Equation 11 describes the permeability-porosity relationship of a packed column of same-sized particles through which the flow is laminar, where κ_0 and $\varnothing_0$ are the initial permeability and porosity, respectively. Equation 11 accounts for geometric changes of the particles, specifically the particle size. For negligible changes in the particle size, asphaltene nanoaggregate adsorptions onto particle surfaces reduce $\varnothing$, and hence r_H decreases according to Eq. 7. Thus, Eq. 11 approximates the influence of pore throat constriction on the permeability. The Civan's power-law flow unit equation, given by[49,55,56,59–62]

$$\sqrt{\frac{k}{\varnothing}} = \Gamma\left(\frac{\varnothing}{\alpha-\varnothing}\right)^{\beta} \tag{12}$$

describes changes in a packed column of particles where laminar flow induces the mechanical entrapment of ultrafine particles via pore throat plugging (e.g., hydrodynamic bridging). Here, Γ and β are the exponent and interconnectivity parameters, and α is the cement exclusion factor ($\alpha = 1-\alpha_c$, where α_c is the volume fraction of the cementation or grain consolidation in porous media). The values of the parameters

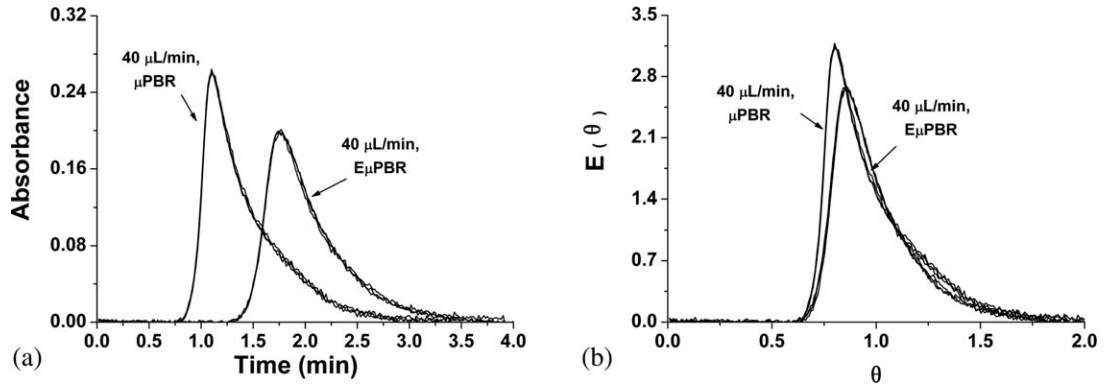

Figure 4. Measured RTDs of *n*-heptane injected into EμPBR and μPBRs.

(a) Absorbance as a function of time in EμPBR and μPBRs and (b) comparison of $E(\theta)$ values as a function of dimensionless time (θ) in EμPBRs and μPBRs.

vary in the range of $\Gamma \geq 0$, $0 \leq \beta < \infty$, and $\varnothing < \alpha \leq 1.0$. For convenience in the plotting of the dimensionless permeability and porosity data, Eq. 12 can be expressed by[49,55,62]

$$\sqrt{\frac{k/k_0}{\varnothing/\varnothing_0}} = \Gamma \sqrt{\frac{\varnothing_0}{k_0}} \left(\frac{\varnothing/\varnothing_0}{(\alpha/\varnothing_0)-(\varnothing/\varnothing_0)} \right)^{\beta} \tag{13}$$

The best estimate values of the parameters Γ and β are determined using Supporting Information Eq. S1 by means of the least-squares fit of the experimental data of permeability and porosity, provided that Γ and β vary, whereas α is approximately constant. Either Eq. 11 or 13, as will later be shown, yields insight on asphaltene deposition mechanisms within μPBR.

Effect of migration of fine particles on permeability impairment and porosity loss in porous media can be estimated by calculating the dispersion coefficient of particles migrating in the flowing phase, D, by[63]

$$D = 8.8\, u_i \varnothing d_P \tag{14}$$

It is important to note that d_P here is the size of grain particles, not the size of deposition particles in the bulk flow.

Vogel–Tammann–Fulcher equation

The Vogel–Tammann–Fulcher (VTF) equation has been widely used to correlate the temperature dependent parameters of various physical and chemical processes, such as diffusivity, viscosity, emulsion stability, and wettability related properties of porous media, among others.[64–66] The general VTF equation, as described by Civan, is expressed as[64,65]

$$\ln f = \ln f_c - \frac{E}{R(T-T_c)} \tag{15}$$

where T and T_c are the actual and critical-limit absolute temperatures of the system, separately. Here, E is the activation energy of the system, R is the universal gas constant, f is a temperature dependent parameter, and f_c is the high temperature value of the parameter f in the limit as $(T - T_c) \rightarrow \infty$ (also known as the pre-exponential coefficient). When $T_c = 0$, Eq. 14 is converted into the Arrhenius expression. As will be shown in the next section, the experimental data of asphaltene solubility in mixture of 40.0 vol % toluene-60.0 vol % *n*-heptane, S, and permeability impairment, $\kappa_{damage}/\kappa_{initial}$, will be correlated using VTF equation to elucidate the temperature dependence.

Results and Discussion

Characterization of μPBRs

Understanding asphaltene accumulation in μPBRs begins with first principle characterizations of the microsystems themselves. Supporting Information Table S1 summarizes the experimental conditions and the characteristic dimensionless quantity estimates for the empty microreactor (EμPBR). From Supporting Information Table S1, Reynolds number (Re) of 1.02 (for flow rates of 40.00 μL/min) confirms the flow was laminar, whereas Capillary numbers (Ca) on the order of 10^{-5} and a Weber number (We) of 0.38×10^{-5} support that surface tension forces dominated instead of the inertial forces. The dimensionless quantity estimates for the EμPBR, exhibiting characteristic length scales of an order of magnitude larger than those anticipated within the packed-bed, elucidate that surface tension forces will also dominate during flow through the packed-bed of quartz particles. From the micrograph and the distribution of Figures 2d, e, the quartz particles were measured to range from 20 to 40 μm. The corresponding minimum characteristic aspect ratio of the microchannel height-to-particle size is 7.5, which ensured that convective jamming was avoided[34] while injecting a quartz slurry (i.e., quartz particles suspended in absolute ethanol) with 5-mL glass syringes. The resultant μPBR loaded with quartz particles was used as the best case (i.e., free of asphaltene accumulations) for all experiments.

RTDs were next measured to determine the porosity within the μPBR. The tracer, 1.0 μL 20.0 vol % acetone in *n*-heptane injected in-line into the carrier *n*-heptane solvent, was analyzed downstream via UV-Vis spectroscopy (see Figure 3). Figure 4 gives the RTD measurements [the absorbance and the dimensionless RTD, $E(\theta)$] during *n*-heptane flow in both EμPBR and μPBRs. Mean residence times of 2.01 ± 0.01 and 1.33 ± 0.01 min for EμPBR and μPBRs were estimated for flow rates of 40.00 μL/min, respectively (see Figure 4a). The corresponding mean volume (obtained from RTD measurements) was 80.2 ± 0.5 μL for the EμPBR and 53.1 ± 0.3 μL for the μPBR. The volume difference of 27.1 μL, the volume occupied by quartz particles, estimates the porosity of the packed-bed to be 39.7%. Based on this porosity and a mean particle size, d_R, of 29 μm, the actual fluid velocity, u_i, (calculated by Eq. 4) and Reynolds number in the packed-bed, Re_P, (from Eq. 6) are reported in Supporting Information Table S1. Values of $u_i = 6.17 \times 10^{-4}$ m/s were estimated to be larger than the mean velocity, $u = 2.46 \times$

Table 1. Characteristics of Quartz μPBRs Estimated by Their RTDs

Reactor	V (μL)	$\varnothing_{RTD}$ (%)	m (mg)	$\varnothing_{mass}$ (%)	κ ($\times 10^{-13}$ m^2)	$\mathcal{T}$	r_H (μm)
EμPBR	80.20	–	0	–	–	1	–
μPBR 1	53.07	39.7	72.5	39.2	5.18	1.71	3.12
μPBR 2	53.52	40.7	71.8	39.8	5.53	1.69	3.20
μPBR 3	53.19	40.0	72.7	39.0	5.40	1.71	3.09
μPBR 4	53.58	40.8	71.4	40.1	5.53	1.68	3.24

10^{-4} m/s, within the EμPBR. Values of $Re_P = 2.76 \times 10^{-2}$ confirm laminar flow, as expected.

Dispersion within the μPBR was characterized by analyses of the $E(\theta)$ values of Figure 4b. Maximum $E(\theta)$ peak height values of 3.13 for μPBR and 2.66 for EμPBR yield estimations of (D^*/uL) from Eq. 8. As shown in Supporting Information Table S2, $(D^*/uL) = 1.34 \times 10^{-2}$ for the EμPBR and 1.03×10^{-2} for the μPBR. As a consequence, the μPBR experienced reduced axial dispersion compared to the EμPBR for the same injection rate of 40.00 μL/min. Molecular diffusivity $\mathcal{D}$ values were calculated (from Eq. 10) to be 0.85×10^{-8} m^2/s in the EμPBR and of similar magnitude (0.32×10^{-8} m^2/s) as in the μPBR, based on values of Bo obtained from Eq. 9. Values of $Bo = 52$ in the EμPBR and 225 in μPBR were significantly less, as expected, than those previously reported in the range of 10^3 to 10^4 for ~150-μm microchannels.[33] One further observes $E(\theta)$ values of Figure 4b shift to the left for the μPBR compared to the EμPBR. These shifts indicate some degree of recirculation eddies within the μPBR.[67] In all scenarios, however, convection dominates over molecular diffusion.

Reproducibility was next evaluated by reloading the EμPBR with fresh quartz particles four times, each separately, and the resultant porosities determined by RTD ($\varnothing_{RTD}$). Table 1 reports the characteristics of each packed-bed. Values of $\varnothing_{RTD}$, as seen in Table 1, ranged from 39.7 to 40.8%. The masses of quartz particles within each microreactor were also measured, and the corresponding porosity ($\varnothing_{mass}$) estimated from 39.2 to 40.1%. Pressure drop measurements estimate the permeability ~5.5×10^{-13} m^2 by Eq. 1 and the tortuosity ~1.7 given by Eq. 6. The hydraulic radius estimated by Eq. 8 reveals pore throats of ~6.4 μm.

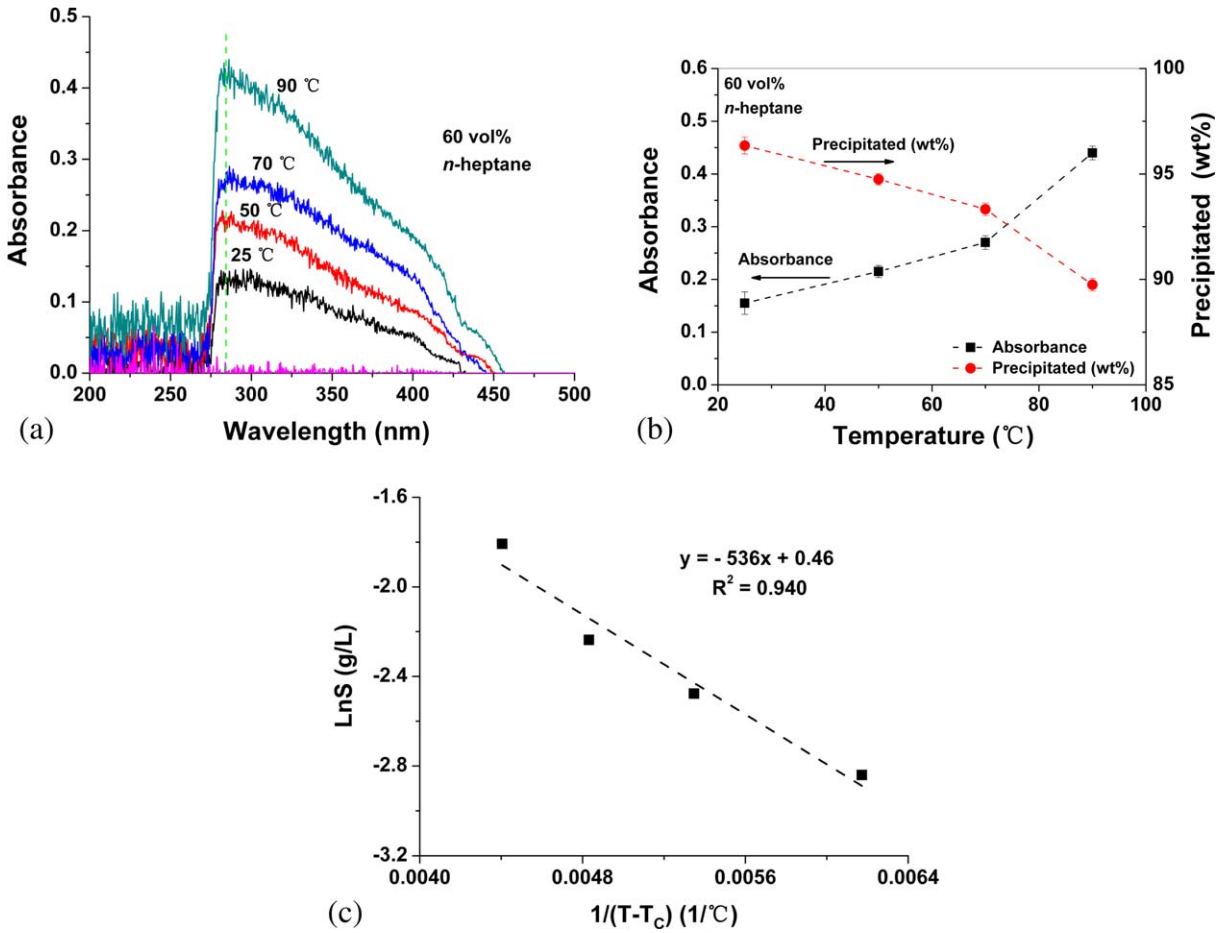

Figure 5. (a) UV-Vis absorbance of asphaltenes in 40 vol % toluene-60 vol % *n*-heptane filtrates. (b) Precipitated wt % of asphaltenes recovered by filtration, and their corresponding absorbance at 286 nm at different operating temperatures. (c) Semilog linear plot of the asphaltene solubility in toluene and *n*-heptane mixture as a function of reciprocal of temperature deviation from the critical-limit temperature value.

[Color figure can be viewed in the online issue, which is available at wileyonlinelibrary.com.]

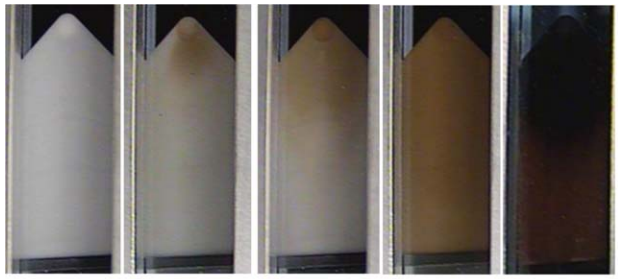

Figure 6. Photographs of the μPBR during asphaltene accumulations for different pore volumes injected, t/τ_P, obtained by CCD camera.

In all scenarios, parameter estimates demonstrate conclusively that reloading the packed-beds with quartz particles is highly reproducible.

Influence of temperature on asphaltene accumulation

The solubility of asphaltenes in mixtures of 40.0 vol % toluene-60.0 vol % *n*-heptane at 25.0, 50.0, 70.0, and 90.0°C were investigated, each separately, to delineate the role of temperature on accumulation in μPBRs. Mixtures of 2.4-mL *n*-heptane and 1.6-mL toluene (with 4 g/L asphaltenes) were agitated in 20-mL vials for 24 h at each temperature and the insoluble fractions separated using Whatman No. 3 filter paper. The absorbances of asphaltenes in the filtrates were then measured using UV-Vis spectroscopy, as shown in Figure 5a, for each temperature condition. As can be seen, the absorbance wavelengths range from 275 to ~450 nm with maxima of 286 nm for all temperatures. Figure 5b illustrates the absorbance maxima (at 286 nm) increased over the temperature range, whereas the mass of the recovered precipitate decreased (i.e., the mass difference before and after filtration). The relationship between the UV-Vis absorbance of light and the asphaltenes concentration in the filtrate was useful in identifying the solubility. At 90.0°C, 89.7 wt % of asphaltenes precipitated, and the value increased to 96.3 wt % at 25.0°C. The solubility of asphaltenes in mixtures of 40 vol % toluene-60 vol % *n*-heptane obviously increased as the temperature increased, which is consistent with the work of others.[6] Figure 5c is the semilog linear plot of asphaltene solubility as a function of reciprocal of temperature deviation from the critical-limit temperature. Pre-exponential coefficient S_c, E/R, and T_c were determined to be 1.58 g/L, 536 K, and 136 K (−137°C), respectively. The results of Figure 5 were essential to successfully precipitate asphaltenes within the interstitial pore spaces of μPBRs.

Asphaltenes were next precipitated within μPBRs for each temperature ranging from 25.0 to 90.0°C. As shown in Figure 2f, 4 g/L asphaltenes in toluene and *n*-heptane were injected (at constant flow rates of 16.00 and 24.00 μL/min) into the μPBR of 35 kPa backpressure. The visual observations of the 70.0°C packed-beds of Figure 6 (obtained using a CCD camera) are noteworthy. The native packed-bed of porosity 39.8% was gradually damaged (from left to right in Figure 6) as the number of pore volumes injected, t/τ_P, increased from 0 to 68.0. No significant channeling is evident from the color gradients of Figure 6. Interestingly, the inlet color was similar to the outlet after injecting >1.0 pore volume, which supports that asphaltene accumulation was uniform throughout the packed-bed. Accumulations that impair the permeability are expected to increase fluidic resistances, and hence pressure drops according to Eq. 1. As shown in Figure 7, the dimensionless pressure drop, $\Delta P/\Delta P_0$, increased as a function of the pore volumes of 4 g/L asphaltenes in toluene injected.

Gradual increases in $\Delta P/\Delta P_0$ were initially observed with increasing t/τ_P for values <45. The steady $\Delta P/\Delta P_0$ increases and oscillations $>\pm 1$ (leading up to about 45 pore volumes) indicate the adsorption and desorption of asphaltenes onto and from the quartz particle's surfaces, as supported by Supporting Information Figure S1. Adsorption and desorption overlap with bulk kinetic processes. As deposition occurred in the packed-bed, the actual velocity increased continuously (from $u_i = 6.0 \times 10^{-4}$ m/s calculated by Eq. 4), especially near the inlet where supersaturation ratios are at their maxima. Once the critical actual velocity was obtained ($\sim 6.0 \times 10^{-3}$ m/s),[68] at which point deposited asphaltenes desorbed from the quartz particle's surfaces by inertial forces, the dimensionless pressure drop decreased and migration in the direction of flow of the precipitated asphaltenes occurred. Temperature clearly plays a role in the accumulation process as increasing the temperature from 25.0 to 90.0°C reduced the number of pore volumes for the differential to approach infinity. As an example, less pore volumes were needed at 90.0°C to obtain the same dimensionless pressure drop of 225 at a temperature of 25.0°C. These observations arise from the fact that the apparent onset time is reduced at higher temperatures,[6] and larger asphaltenes precipitate in the same time scale.[6] As a result, hydraulic channels of the porous media were "turned-off" and significant pressure buildups occurred in shorter relative time scales. The results of Figure 7 undergird that injections designed using Figure 5 indeed successfully damaged the μPBRs. The extents of the damages are summarized in Table 2. The packed-bed surfaces experience infinite residence time where apparent "onset" precedes mechanical entrapment, which occurs when the asphaltenes are sufficiently small to undergo adsorption and desorption without

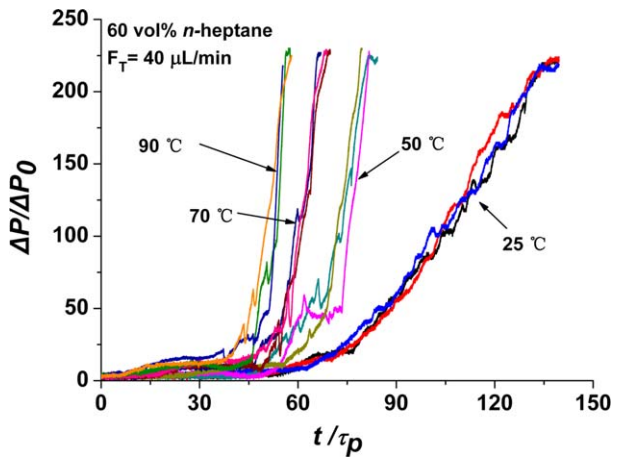

Figure 7. Influence of temperature on the dimensionless pressure drop as a function of the pore volumes of 4 g/L asphaltenes in toluene injected.

[Color figure can be viewed in the online issue, which is available at wileyonlinelibrary.com.]

Table 2. Influence of Temperature (*n*-Heptane 60.0 vol %) on μPBR Impairments

Test	t/τ_P	T (°C)	$\varnothing_{initial}$ (%)	$\kappa_{initial}$ ($\times 10^{-13}$ m^2)	m_{total} (mg)	m_{waste} (mg)	$m_{deposited}$ (mg)	$\frac{\varnothing_{damage}}{\varnothing_{initial}}$	$\frac{\kappa_{damage}}{\kappa_{initial}}$	s ($\times 10^3$)	$\frac{\Delta P}{\Delta P_0}$
1	56.0	90.0	39.7 ± 0.92	5.18 ± 0.066	4.0	3.4 ± 0.05	0.6	0.972	0.005	3.58	225
2	56.0	70.0	40.7 ± 0.80	5.53 ± 0.051	4.1	3.6 ± 0.10	0.5	0.977	0.020	0.75	50
3	56.0	50.0	40.0 ± 0.70	5.40 ± 0.046	4.0	3.5 ± 0.03	0.5	0.977	0.051	0.25	20
4	56.0	25.0	40.8 ± 0.22	5.53 ± 0.022	4.1	3.7 ± 0.11	0.4	0.982	0.145	0.07	6.9
5	68.0	70.0	39.7 ± 0.59	5.13 ± 0.043	4.9	3.8 ± 0.19	1.1	0.949	0.005	3.07	225
6	68.0	50.0	41.0 ± 0.54	5.58 ± 0.039	5.0	4.1 ± 0.15	0.9	0.959	0.021	0.62	49
7	68.0	25.0	40.9 ± 0.38	5.54 ± 0.037	5.0	4.3 ± 0.12	0.7	0.968	0.063	0.16	16
8	81.0	50.0	41.1 ± 0.76	5.68 ± 0.054	6.0	4.3 ± 0.20	1.7	0.923	0.005	2.82	225
9	81.0	25.0	40.2 ± 0.13	5.59 ± 0.019	5.9	4.8 ± 0.09	1.1	0.949	0.028	0.36	36
10	139	25.0	39.9 ± 0.48	5.16 ± 0.037	10.0	7.0 ± 0.15	3.0	0.860	0.005	2.07	225

significant surface or body forces acting on the nanoparticles, relative to particle-to-surface and particle-to-particle attraction. Nanoaggregation kinetics is clearly a key in the deposition mechanism.

At lower temperatures (e.g., 25.0°C), a larger number of precipitated asphaltenes (smaller in size) flowed the same axial distance until deposition occurred (i.e., ease of penetration into the porous media). Furthermore, submicron particles undergo Brownian diffusion, which can play an important role in the process of particle transport to a pore's surfaces.[68] The overall outcome was less impairment at 25.0°C as compared to experiments performed at higher temperatures, which is confirmed by the results of Table 2. Here, the porosity damage, $\varnothing_{damage}/\varnothing_{initial}$, was directly calculated from the measured mass of deposited asphaltenes (obtained by performing component mass balances and from the previously reported asphaltene S.G. = 1.2).[1] Table 2 also gives permeability impairment values, $\kappa_{damage}/\kappa_{initial}$ = 0.005–0.145, calculated from Eq. 1 and the van Everdingen–Hurst Skin Factor, $s = (0.07–3.58) \times 10^3$, estimated from Eq. 2. The results support that μPBRs were successfully engineered and damaged by asphaltene accumulations.

RTDs were next measured to validate the porosity damage calculations and to characterize dispersion within the damaged packed-bed microreactors (DμPBRs). As before, the tracer, 1.0 μL 20.0 vol % acetone in *n*-heptane injected inline into the carrier *n*-heptane (100 vol %) solvent, was analyzed downstream via UV-Vis spectroscopy (see Figure 3). Figure 8 reports RTD measurements for native μPBR and DμPBRs damaged after injecting 81.0 pore volumes of 4 g/L asphaltenes in toluene (60.0 vol % *n*-heptane) at 25.0°C. The corresponding mean volume difference of 0.85 μL (between the μPBR and the DμPBRs), described by the dashed-line shift in Figure 8a, estimates $\left(\varnothing_{damage}/\varnothing_{initial}\right)_{RTD} = 0.952$. Comparison to the calculated value of 0.949 from Table 2 (Test 9) demonstrates excellent agreement between the mass balance approach and measurement of RTDs. Based on the measured RTD porosity and a mean particle size, d_R, of 29 μm, the actual fluid velocity, u_i, (calculated by Eq. 4) and Reynolds number in the packed-beds, $Re_{P(RTD)}$, (from Eq. 6) are reported in Table 3.

Values of $u_i = (1.54–15.4) \times 10^{-4}$ m/s are less than the critical actual velocity, $u_i = 60.0 \times 10^{-4}$ m/s for Reynolds number in the range of 0.54 and 5.38 $\times 10^{-2}$. Dispersions within the μPBR and the DμPBRs for all *Re* values were characterized by analyses of the $E(\theta)$ values of Figure 8b. As shown in Table 3, (D^*/uL) was estimated to range from (0.86–1.20) $\times 10^{-2}$ for the μPBR and from (0.74–1.13) $\times 10^{-2}$ for the DμPBR. As a consequence, the deposition of asphaltenes reduced axial dispersion for the same *Re* values. Values of *Bo* were estimated to range from 56 to 560 in the μPBR and from 53 to 550 in DμPBRs, which confirms that convection dominated over molecular diffusion for all experiments. Furthermore, no obvious channeling occurred in the μPBR or the DμPBRs, as in each case only a single dominant $E(\theta)$ peak was detectable (see Figure 8b).[50]

Influence of n-*heptane composition*

The role of *n*-heptane composition on the deposition was examined to further comprehend the stability of asphaltenes in μPBRs. The continuous, high-throughput, and integrated system enabled screening of the *n*-heptane compositional

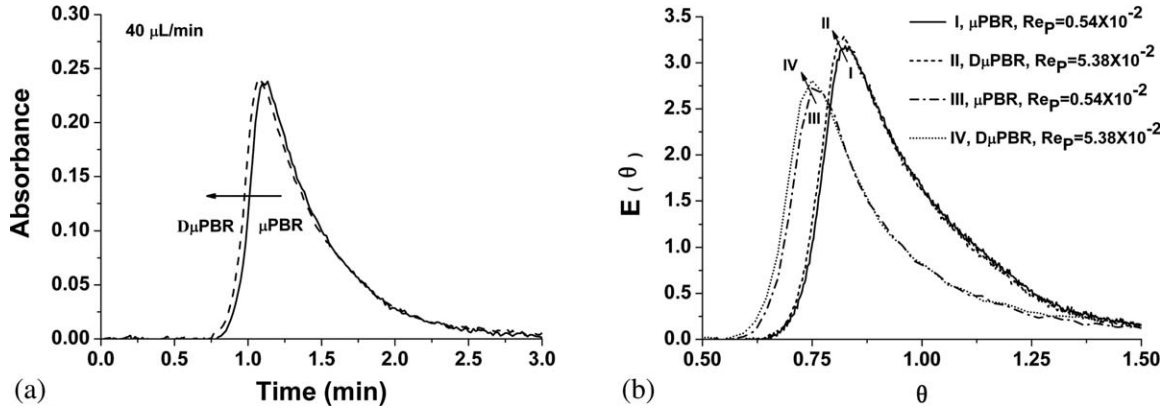

Figure 8. RTD measurements of *n*-heptane flow in μPBR and DμPBRs.

(a) Absorbance as a function of time at 40.00 μL/min and (b) comparison of $E(\theta)$ values as a function of dimensionless time (θ) for Reynolds number of 0.54 and 5.38 $\times 10^{-2}$ in μPBR and DμPBRs.

Table 3. Dispersion in μPBR and DμPBRs Estimated by Their RTDs

	u_i ($\times 10^{-4}$ m/s)	$Re_{P(RTD)}$ ($\times 10^{-2}$)	σ^2 (min^2)	σ_θ^2	$D^*/(uL)$	D^* ($\times 10^{-8}$ m^2/s)	Bo
(a) μPBR	1.54	0.54	1.51	0.018	0.0086	2.12	56
	15.4	5.38	0.04	0.025	0.0120	31.4	560
(b) DμPBR	1.54	0.54	1.42	0.015	0.0074	2.03	53
	15.4	5.38	0.04	0.024	0.0113	29.6	550

influence (from 0 to 90.0 vol %) on asphaltene solubility using the approach previously described for temperatures of 25.0–90.0°C (refer to Figures 3 and 5). Figure 9a reports the asphaltenes absorbance at 286 nm in toluene-*n*-heptane filtrates. As anticipated, the absorbance decreased and the precipitation wt % increased with increasing *n*-heptane vol % as the solubility decreased at constant 70.0°C. The solubility reported in Figure 9a were then analyzed to successfully precipitate asphaltenes within the interstitial pore spaces of μPBRs for varying *n*-heptane compositions.

Using data of Figure 9a, Asphaltenes were next precipitated within μPBRs for each *n*-heptane composition, ranging from 50.0 to 80.0 vol % at constant temperature of 70.0°C. As shown in Figure 9b, $\Delta P/\Delta P_0$ values increased as a function of the pore volumes of 4 g/L asphaltenes in toluene injected. Similar to the influence of the temperature, gradual increases in $\Delta P/\Delta P_0$ were initially observed with increasing t/τ_P for values <30 prior to abrupt increases toward differential infinity. The general trend of Figure 9b is consistent with the results of Figure 9a: increasing the *n*-heptane vol % incrementally (from 50.0, 60.0, 70.0, to 80.0 vol %) reduced the asphaltene solubility and precipitation onset time, and hence impairments of packed-beds occur in shorter relative time scales. The trends of Figure 9b were observed to be highly reproducible. Remarkably, no obvious pressure buildup was observed for an *n*-heptane composition of 40 vol % from 0 to 350 pore volumes of 4 g/L asphaltene in toluene injected, which elucidates a critical concentration of *n*-heptane is a necessary condition to deposit asphaltenes in the quartz μPBRs.

The extents of the impairments for different *n*-heptane vol % are summarized in Table 4. The analogous trends hold, from varying the packed-bed temperature, to increasing the *n*-heptane vol %. At lower *n*-heptane compositions (e.g., 50.0 vol %), a larger number of precipitated asphaltenes (smaller in size) likely flowed the same axial distance until deposition occurred, and any submicron particles logically experienced transport to the quartz particle's surfaces via Brownian diffusion.[68] The overall outcome was less impairment in 50.0 vol % *n*-heptane (for the same pore volumes injected) as compared to experiments performed in larger compositions, as confirmed by the porosity damage ($\varnothing_{damage}/\varnothing_{initial}$), permeability impairment ($\kappa_{damage}/\kappa_{initial}$), and the van Everdingen–Hurst Skin Factor (s) estimations reported in Table 4. The *n*-heptane composition clearly influenced impairment, and the damage mechanism appeared to be the same in all scenarios.

Influence of n-*alkane carbon number*

Hydrocarbon producing reservoirs are comprised of a vast range of aromatic and straight-chain compounds, which vary widely in their intrinsic chemical and physical properties. A common parameter used to evaluate crude oil systems is the carbon number of alkanes. Next, the role of *n*-alkane carbon number, X, from *n*-C_5 to *n*-C_9, on asphaltene depositions in μPBRs is elucidated using the same high-throughput approach engineered to study temperature and *n*-heptane compositional influences.

Figure 10 summarizes measured asphaltene solubility and dimensionless pressure drops during injections of different *n*-alkanes (as cosolvents) into μPBRs. In Figure 10a, analyses of UV-Vis absorbances of asphaltenes in filtrates (at 286 nm) demonstrates that increasing the carbon number, sequentially from 5 to 9, as expected, increased their solubility. The same trends were observed at 25.0 and 70.0°C. Measurements of the solubility proved useful in assessing the role of the carbon number on the impairment of μPBRs. Figure 10b reports that $\Delta P/\Delta P_0$ values increased as a

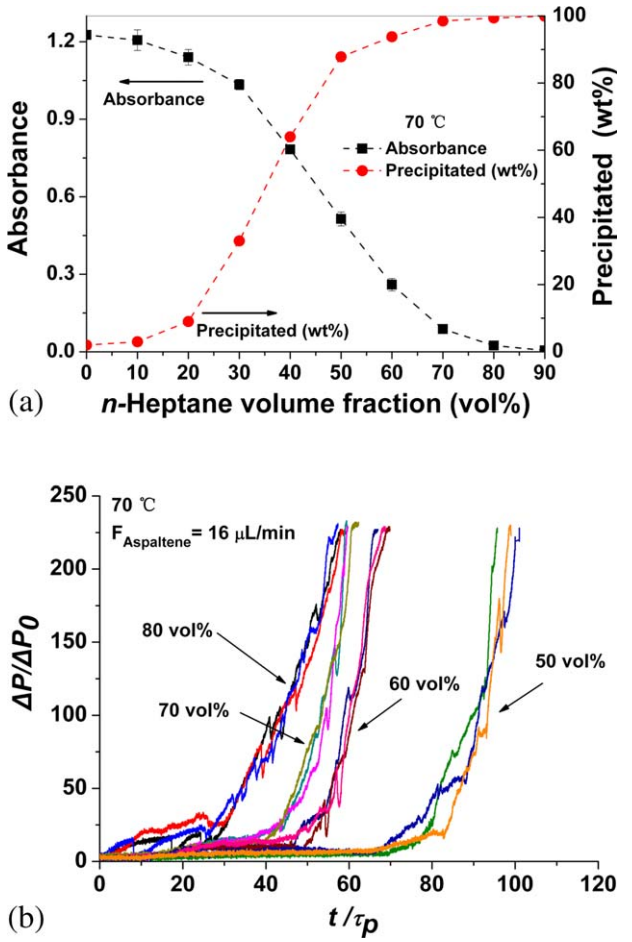

Figure 9. Analysis of the influence of *n*-heptane composition.

(a) Precipitated wt % of asphaltenes (in the filtrates) and their corresponding absorbance at 286 nm at different *n*-heptane compositions. (b) Influence of *n*-heptane vol % on the dimensionless pressure drop as a function of pore volumes of 4 g/L asphaltenes in toluene injected.

[Color figure can be viewed in the online issue, which is available at wileyonlinelibrary.com.]

Table 4. Influence of *n*-Heptane Composition on μPBR Impairments

Test	t/τ_P	*n*-Heptane (vol %)	$\varnothing_{initial}$ (%)	$\kappa_{initial}$ ($\times 10^{-13}$ m^2)	m_{total} (mg)	m_{waste} (mg)	$m_{deposited}$ (mg)	$\frac{\varnothing_{damage}}{\varnothing_{initial}}$	$\frac{\kappa_{damage}}{\kappa_{initial}}$	s ($\times 10^3$)	$\frac{\Delta P}{\Delta P_0}$
1	40.0	80.0	40.7 ± 0.13	5.50 ± 0.018	2.9	2.6 ± 0.04	0.3	0.986	0.030	0.51	65
2	40.0	70.0	40.1 ± 0.48	5.23 ± 0.041	2.9	2.7 ± 0.11	0.2	0.991	0.073	0.21	19
3	40.0	60.0	39.6 ± 0.87	5.14 ± 0.066	2.9	2.7 ± 0.09	0.2	0.991	0.091	0.15	11
4	40.0	50.0	41.5 ± 0.31	5.75 ± 0.028	3.0	2.9 ± 0.13	0.1	0.996	0.145	0.11	5.5
5	58.0	80.0	40.7 ± 0.52	5.58 ± 0.038	4.3	3.7 ± 0.04	0.6	0.972	0.009	1.72	225
6	58.0	70.0	40.5 ± 0.82	5.33 ± 0.061	4.3	3.6 ± 0.16	0.7	0.968	0.008	1.96	164
7	58.0	60.0	40.5 ± 0.64	5.48 ± 0.056	4.3	3.7 ± 0.14	0.6	0.972	0.016	0.96	64
8	58.0	50.0	39.9 ± 0.52	5.23 ± 0.046	4.2	4.0 ± 0.25	0.2	0.991	0.130	0.11	5.9
9	68.0	60.0	39.7 ± 0.59	5.13 ± 0.044	4.9	3.8 ± 0.16	1.1	0.949	0.005	3.07	225
10	68.0	50.0	40.5 ± 0.40	5.44 ± 0.036	4.9	4.4 ± 0.19	0.5	0.977	0.080	0.17	10
11	99.0	50.0	40.3 ± 0.39	5.33 ± 0.041	7.2	5.6 ± 0.47	1.6	0.926	0.004	3.67	225

function of the pore volumes of 4 g/L asphaltenes in toluene-*n*-pentane (*n*-C_5) injected. However, reproducibility at 70.0°C was evidently compromised, as shown by the ~90 pore volume difference for the same conditions. This observation is attributed to the lower bubble point of *n*-pentane (36.0°C at atmospheric pressure, from Supporting Information Table S3) compared to other *n*-alkanes studied. Packed-bed inlet pressures near 690 kPa dropped to 35 kPa, and thus flashing of the cosolvent introduced variability of $\Delta P/\Delta P_0$ values (i.e., the volume of ideal vapor near atmospheric conditions is ~2 orders of magnitude > the volume of the same component in the liquid phase). As shown in Figure 10c, increasing the carbon number from 5 to 6 by injecting *n*-hexane as the cosolvent reduced, but did not eliminate altogether, the variability of $\Delta P/\Delta P_0$ values, which is explained by its bubble point of 69°C from Supporting Information Table S3. Figure 10d, however, illustrates that solvent flashing was avoided for carbon numbers >7, as $\Delta P/\Delta P_0$ values increased with excellent reproducibility as a function of the pore volumes of 4 g/L asphaltenes in toluene injected in the presence of *n*-heptane (*n*-C_7), *n*-octane (*n*-C_8), and *n*-nonane (*n*-C_9). Similar to the influence of the temperature and the *n*-heptane composition, gradual increases in $\Delta P/\Delta P_0$ were initially observed with increasing t/τ_P for values <40 before abrupt increases toward differential infinity. Perhaps just as intriguing, increasing the *n*-alkane carbon

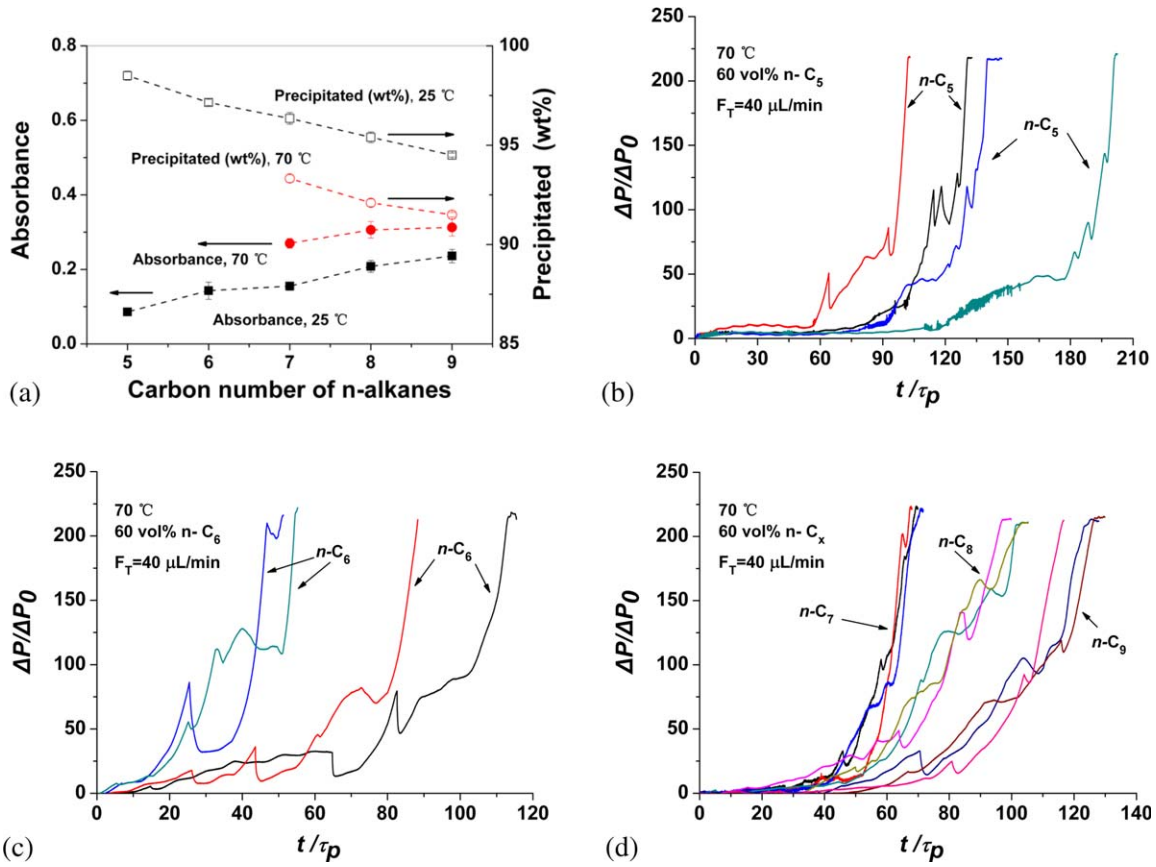

Figure 10. Analysis of the influence of *n*-alkane carbon number.

(a) Precipitated wt % of asphaltenes (in the filtrates), and their corresponding absorbance at 286 nm as a function of *n*-alkane carbon number. Influence of (b) *n*-pentane, (c) *n*-hexane, and (d) *n*-heptane, *n*-octane, and *n*-nonane on the dimensionless pressure drop as a function of pore volumes of 4 g/L asphaltenes in toluene injected. [Color figure can be viewed in the online issue, which is available at wileyonlinelibrary.com.]

Table 5. Influence of *n*-Alkane (*n*-C_x) on μPBR Impairments

Test	t/τ_P	*n*-C_X	$\varnothing_{initial}$ (%)	$\kappa_{initial}$ ($\times 10^{-13}$ m^2)	m_{total} (mg)	m_{waste} (mg)	$m_{deposited}$ (mg)	$\frac{\varnothing_{damage}}{\varnothing_{initial}}$	$\frac{\kappa_{damage}}{\kappa_{initial}}$	s ($\times 10^3$)	$\frac{\Delta P}{\Delta P_0}$
1	68.0	*n*-C_7	39.7 ± 0.59	5.13 ± 0.044	4.9	3.8 ± 0.16	1.1	0.949	0.005	3.07	225
2	68.0	*n*-C_8	40.1 ± 0.47	5.21 ± 0.049	4.9	4.5 ± 0.27	0.4	0.982	0.017	0.81	60
3	68.0	*n*-C_9	40.7 ± 0.62	5.56 ± 0.054	5.0	4.8 ± 0.31	0.2	0.991	0.056	0.20	18
4	100	*n*-C_8	39.1 ± 0.35	5.08 ± 0.046	7.0	5.9 ± 0.33	1.1	0.948	0.005	3.18	220
5	100	*n*-C_9	40.1 ± 0.52	5.22 ± 0.034	7.2	6.8 ± 0.45	0.4	0.982	0.014	0.74	70
6	130	*n*-C_9	40.7 ± 0.64	5.53 ± 0.039	9.5	8.2 ± 0.39	1.3	0.941	0.005	2.25	200

number (sequentially from 7, 8, to 9) increased the asphaltene solubility and extended the precipitation onset time, and hence impairments of packed-beds were belated. The extents of the impairments for different *n*-alkane carbon number from *n*-C_5 to *n*-C_9 are summarized in Table 5 and Supporting Information Table S4.

The overall outcome was less impairment in 60.0 vol % *n*-nonane (for the same pore volumes injected) as compared to experiments performed in *n*-octane or *n*-heptane, as confirmed by the porosity damage ($\varnothing_{damage}/\varnothing_{initial}$), permeability impairment ($\kappa_{damage}/\kappa_{initial}$), and the van Everdingen–Hurst Skin Factor (s) estimations tabulated in Table 5. The results undergird that the carbon number plays a key role in the impairment of quartz μPBRs. In all scenarios of temperature, *n*-heptane composition, and *n*-alkane carbon number changes, the damage mechanisms appeared to be universal, which prompted further analyses of the permeability-porosity relationships.

Permeability–porosity relationship

The experimentally determined permeability–porosity relationships for all conditions were compared to Eq. 11[49,55,56] and the Civan's power-law flow unit, Eq. 13,[49,55,62] and the results are illustrated in Figure 11. Equation 11 did not accurately describe the asphaltenes-induced permeability impairment as a function of the porosity impairment. Figure 11a reveals that Eq. 11 overpredicted experimentally measured $\kappa_{damage}/\kappa_{initial}$ values by an order of magnitude for all temperature (from Table 2), *n*-heptane composition (from Table 4), and *n*-alkane (from Table 5) conditions. One can infer from Figure 11a that the damage mechanism did not accurately emulate changes in the quartz particle's sizes within μPBRs, which points to impairment mechanisms other than constriction brought about by asphaltene particle adsorption. Figure 11b instead reveals that mechanical entrapment of asphaltene particles likely dominated the impairment mechanism for all scenarios. The cement

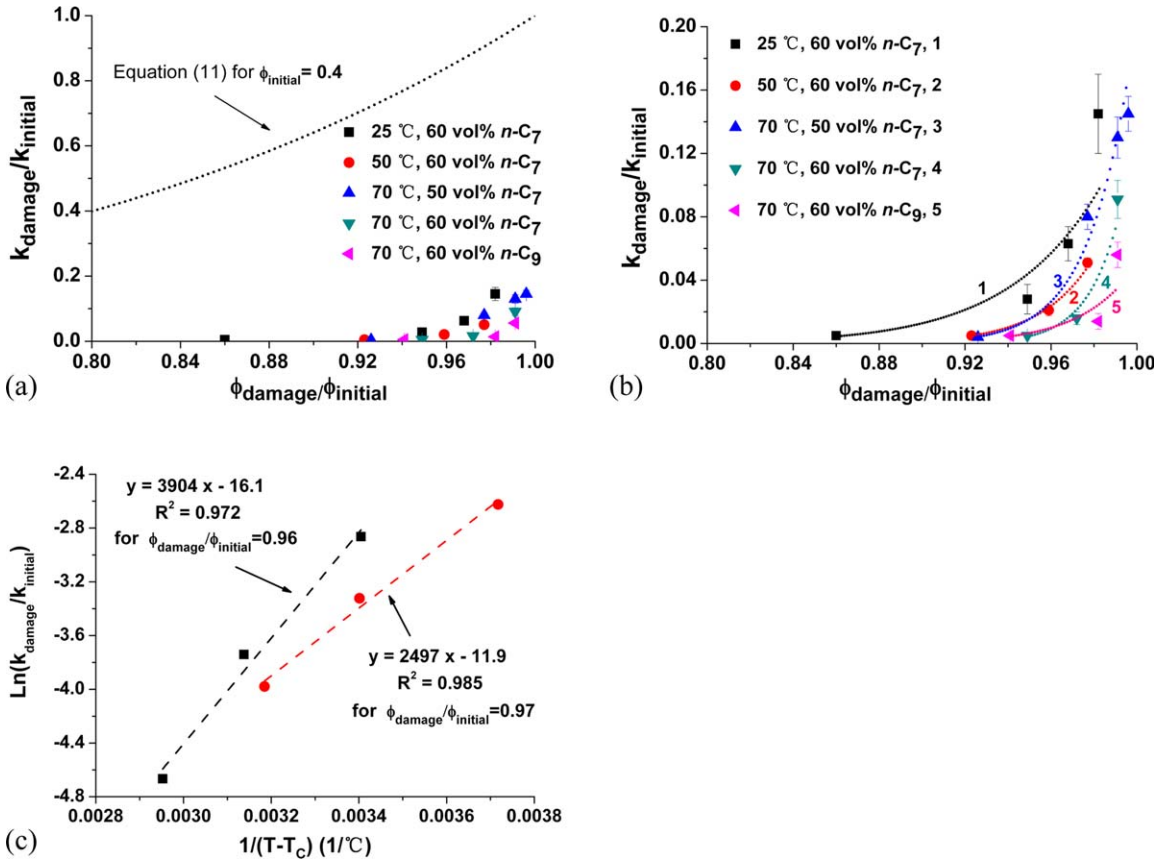

Figure 11. (a) Experimentally measured permeability-porosity compared to the (a) Eq. 1111 and (b) Civan's power-law flow unit Eq. 1313. (c) Semilog linear plot of the permeability impairment in porous media as a function of reciprocal of temperature deviation from the critical-limit temperature value.

exclusion factor varies from 0.95 to 1.0 (Supporting Information Table S5), and Γ and β can be determined by least-squares fit of the experimental data using Supporting Information Eq. S1. The correlated plots and the parameters are reported in Supporting Information Figure S2 and Table S5, respectively. Excellent agreement between Eq. 13 and the experimentally measured $\kappa_{damage}/\kappa_{initial}$ values supports that asphaltene depositions generated pore throat blockages, perhaps via hydrodynamic bridging phenomenon. In addition, the experimental data of permeability impairment at different temperatures of 25, 50, and 70°C (see Supporting Information Figure S3) for $\varnothing_{damage}/\varnothing_{initial}$ of 0.96 and 0.97 were correlated using the VTF equation, as shown in Figure 11c.

The discovery that pore throat blockages dominate the asphaltene accumulation mechanism holds true for the quartz-grain porous media in the present study, and for a broad range of conditions. The existence of clays and other minerals commonly found in siliceous sandstone reservoirs are readily known to influence reservoir surface chemistry. It is quite possible that the compositional heterogeneity of sandstone formations could induce asphaltene nanoaggregate surface attraction, and hence constriction remains as a possible dominant deposition mechanism for permeability impairment. Nanoaggregate repulsion is a problem equally important that could uphold mechanical entrapment as the dominant accumulation mechanism in sandstone reservoirs. Suffice to say that the microchemical analyses reported herein establishes the groundwork for high-throughput chemical and fluidic information that spans the molecular scale to full reservoir production, where enormous libraries of chemical science remain to be discovered.

Conclusions

Conventional and unconventional subterranean reservoirs that are known to produce asphaltenes create the potential for near wellbore skin damage, which results in production losses of considerable economic magnitude. High-throughput packed-bed microreactors were successfully innovated to understand asphaltene accumulation mechanisms. RTDs of the packed bed microreactors before and after loading with quartz particles were measured using in-line UV-Vis spectroscopy. Highly producible, stable packings of quartz particles with porosity of ~40% and permeability of $\sim 5.5 \times 10^{-13}$ m^2 were obtained. Asphaltenes solubility was made readily available via in-line microfluidic analyses for different temperatures, *n*-heptane compositions, and *n*-alkanes. All these three scenarios were observed to influence asphaltenes deposition in the porous media, and reduced dispersion was obtained in the damaged packed-bed. The experimentally determined permeability-porosity relationships for all conditions were compared to the simplified Kozeny–Carman and Civan's permeability-porosity relationships, which revealed mechanical entrapment of asphaltene particles dominated the impairment mechanism. The chemical engineering of such continuous flow, lab-on-chip systems have tremendous merit in oilfield chemistry science where chemical and physical properties are vast and dynamic, unsteady-state conditions routinely exist.

Dimensionless pressure drop analyses and measurements of RTDs of packed-bed microreactors elucidated molecular-to-pore scale mechanistic insights. Asphaltene adsorptions were observed to contribute to pore scale impairments in pure quartz-grain packed-bed microreactors. Theoretical predictions of experimentally measured permeability-porosity relationships proved that mechanical entrapment dominated the asphaltene deposition mechanism for all experimental conditions investigated. No channeling was evident in any experiment, and estimations of the Bodenstein number confirmed that convective forces governed relative to diffusive forces within the interstitial pore spaces. The experimental results undergird that packed-bed microreactors are potentially ubiquitous tools that could bridge the scientific gap between molecular-level events and upstream conventional and unconventional energy productions.

Acknowledgment

The authors gratefully acknowledge Nalco Energy Services and Anadarko Petroleum Corporation for funding.

Literature Cited

1. Juyal P, McKenna AM, Fan T, Cao T, Rueda-Velasquez RI, Fitzsimmons JE, Yen A, Rodgers RP, Wang J, Buckley JS, et al. Joint industrial case study for asphaltene deposition. *Energy Fuels*. 2013;27(4):1899–1908.
2. Acevedo S, Ranaudo MA, García C, Castillo J, Fernandez A, Caetano M, Goncalvez S. Importance of asphaltene aggregation in solution in determining the adsorption of this sample on mineral surfaces. *Colloids Surf A*. 2000;166(1):145–152.
3. Hoepfner MP, Limsakoune V, Chuenmeechao V, Maqbool T, Fogler HS. A fundamental study of asphaltene deposition. *Energy Fuels*. 2013;27(2):725–735.
4. Wang J, Buckley JS, Creek JL. Asphaltene deposition on metallic surfaces. *J Dispers Sci Technol*. 2004;25(3):287–298.
5. Verdier S, Plantier F, Bessières D, Andersen SI, Stenby EH, Carrier H. Study of asphaltene precipitation by Calorimetry. *Energy Fuels*. 2007;21(6):3583–3587.
6. Maqbool T, Srikiratiwong P, Fogler HS. Effect of temperature on the precipitation kinetics of asphaltenes. *Energy Fuels*. 2011;25(2):694–700.
7. Marczewski AW, Szymula M. Adsorption of asphaltenes from toluene on mineral surface. *Colloids Surf A*. 2002;208(1):259–266.
8. Joshi NB, Mullins OC, Jamaluddin A, Creek J, McFadden J. Asphaltene precipitation from live crude oil. *Energy Fuels*. 2001;15(4):979–986.
9. Peramanu S, Singh C, Agrawala M, Yarranton HW. Investigation on the reversibility of asphaltene precipitation. *Energy Fuels*. 2001;15(4):910–917.
10. Buckley JS. Asphaltene deposition. *Energy Fuels*. 2012;26(7):4086–4090.
11. Hammami A, Phelps CH, Monger-McClure T, Little T. Asphaltene precipitation from live oils: an experimental investigation of onset conditions and reversibility. *Energy Fuels*. 2000;14(1):14–18.
12. Mousavi Dehghani SA, Vafaie Sefti M, Mirzayi B, Fasih M. Experimental investigation on asphaltene deposition in porous media during miscible gas injection. *Iran J Chem Chem Eng*. 2007;26(4):39–48.
13. Mullins OC, Sheu EY, Hammami A, Marshall AG. Asphaltenes, Heavy Oils, and Petroleomics, Vol. 1. New York, NY: Springer, 2007.
14. Kocabas I, Islam M, Modarress H. A wellbore model for field-scale modeling of asphaltene plugging. *J Pet Sci Eng*. 2000;26(1):19–30.
15. Almehaideb RA. Asphaltene precipitation and deposition in the near wellbore region: a modeling approach. *J Pet Sci Eng*. 2004;42(2):157–170.
16. Nabzar L, Aguilera M, Rajoub Y. Experimental study on asphaltene-induced formation damage. *SPE International Symposium on Oilfield Chemistry*. The Woodlands, TX, 2005.
17. Leontaritis KJ. Asphaltene near-well-bore formation damage modeling. *J Energy Resour Technol*. 2005;127(3):191–200.
18. Fung G, Backhaus W, McDaniel S, Erdogmus M, America B. To pig or not to pig: the marlin experience with stuck pig. *Offshore Technology Conference*. Houston, TX, 2006.
19. Jensen KF. Microreaction engineering—is small better? *Chem Eng Sci*. 2001;56(2):293–303.
20. Günther A, Jensen KF. Multiphase microfluidics: from flow characteristics to chemical and materials synthesis. *Lab Chip*. 2006;6(12):1487–1503.

21. Hartman RL, Sahoo HR, Yen BC, Jensen KF. Distillation in microchemical systems using capillary forces and segmented flow. *Lab Chip*. 2009;9(13):1843–1849.
22. Hartman RL, Jensen KF. Microchemical systems for continuous-flow synthesis. *Lab Chip*. 2009;9(17):2495–2507.
23. Yen BK, Günther A, Schmidt MA, Jensen KF, Bawendi MG. A microfabricated gas–liquid segmented flow reactor for high-temperature synthesis: the case of CdSe quantum dots. *Angew Chem*. 2005;117(34):5583–5587.
24. Watts P, Wiles C. Recent advances in synthetic micro reaction technology. *Chem Commun*. 2007;(5):443–467.
25. Marre S, Park J, Rempel J, Guan J, Bawendi MG, Jensen KF. Supercritical continuous-microflow synthesis of narrow size distribution quantum dots. *Adv Mater*. 2008;20(24):4830–4834.
26. Hessel V, Löwe H. Organic synthesis with microstructured reactors. *Chem Eng Technol*. 2005;28(3):267–284.
27. Hessel V, Angeli P, Gavriilidis A, Löwe H. Gas-liquid and gas-liquid-solid microstructured reactors: contacting principles and applications. *Ind Eng Chem Res*. 2005;44(25):9750–9769.
28. Haswell SJ, Watts P. Green chemistry: synthesis in micro reactors. *Green Chem*. 2003;5(2):240–249.
29. Geyer K, Gustafsson T, Seeberger PH. Developing continuous-flow microreactors as tools for synthetic chemists. *Synlett*. 2009;2009(15):2382–2391.
30. Jähnisch K, Hessel V, Löwe H, Baerns M. Chemistry in microstructured reactors. *Angew Chem Int Ed*. 2004;43(4):406–446.
31. Pennemann H, Watts P, Haswell SJ, Hessel V, Löwe H. Benchmarking of microreactor applications. *Org Process Res Dev*. 2004;8(3):422–439.
32. Roberge DM, Ducry L, Bieler N, Cretton P, Zimmermann B. Microreactor technology: a revolution for the fine chemical and pharmaceutical industries? *Chem Eng Technol*. 2005;28(3):318–323.
33. Hu C, Herz C, Hartman RL. Microfluidic dispersion of mineral oil-seawater multiphase flows in the presence of dialkyl sulfonates, polysorbates, and glycols. *Green Process Synth*. 2013;2(6):611–623.
34. Hartman RL, Naber JR, Zaborenko N, Buchwald SL, Jensen KF. Overcoming the challenges of solid bridging and constriction during Pd-Catalyzed C−N bond formation in microreactors. *Org Process Res Dev*. 2010;14(6):1347–1357.
35. Hartman RL, Naber JR, Buchwald SL, Jensen KF. Multistep microchemical synthesis enabled by microfluidic distillation. *Angew Chem Int Ed*. 2010;49(5):899–903.
36. Hartman RL. Managing solids in microreactors for the upstream continuous processing of fine chemicals. *Org Process Res Dev*. 2012;16(5):870–887.
37. Hu C, Morris JE, Hartman RL. Microfluidic investigation of the deposition of asphaltenes in porous media. *Lab Chip*. 2014;14(12):2014–2022.
38. Grover WH, von Muhlen MG, Manalis SR. Teflon films for chemically-inert microfluidic valves and pumps. *Lab Chip*. 2008;8(6):913–918.
39. Yoon T-H, Park S-H, Min K-I, Zhang X, Haswell SJ, Kim D-P. Novel inorganic polymer derived microreactors for organic microchemistry applications. *Lab Chip*. 2008;8(9):1454–1459.
40. Knitter R, Liauw MA. Ceramic microreactors for heterogeneously catalysed gas-phase reactions. *Lab Chip*. 2004;4(4):378–383.
41. Fletcher PD, Haswell SJ, Pombo-Villar E, Warrington BH, Watts P, Wong SYF, Zhang X. Micro reactors: principles and applications in organic synthesis. *Tetrahedron*. 2002;58(24):4735–4757.
42. Jensen KF. Silicon-based microchemical systems: characteristics and applications. *MRS Bull*. 2006;31:101–107.
43. Chow AW. Lab-on-a-chip: opportunities for chemical engineering. *AIChE J*. 2002;48(8):1590–1595.
44. Kikutani Y, Horiuchi T, Uchiyama K, Hisamoto H, Tokeshi M, Kitamori T. Glass microchip with three-dimensional microchannel network for 2× 2 parallel synthesis. *Lab Chip*. 2002;2(4):188–192.
45. Kikutani Y, Hibara A, Uchiyama K, Hisamoto H, Tokeshi M, Kitamori T. Pile-up glass microreactor. *Lab Chip*. 2002;2(4):193–196.
46. Costa A. Permeability-porosity relationship: a reexamination of the Kozeny-Carman equation based on a fractal pore-space geometry assumption. *Geophys Res Lett*. 2006;33(2):L02318.
47. Lucia F. Petrophysical parameters estimated from visual descriptions of carbonate rocks: a field classification of carbonate pore space. *J Pet Technol*. 1983;35(03):629–637.
48. Van Everdingen A, Hurst W. The application of the Laplace transformation to flow problems in reservoirs. *Trans AIME*. 1949;186(305):97–104.
49. Civan F. *Reservoir Formation Damage-Fundamentals, Modeling, Assessment, and Mitigation*, 2nd ed. Burlington: Gulf Professional Publishing, 2007.
50. Fogler HS. Elements of Chemical Reaction Engineering. New Jersey: Pearson Education, Inc., 2006.
51. Rhodes M. *Introduction to Particle Technology*, 2nd ed. New Jersey: Wiley, 2008.
52. Yun M, Yu B, Xu P, Wu J. Geometrical models for tortuosity of streamlines in three-dimensional porous media. *Can J Chem Eng*. 2006;84(3):301–309.
53. Shen L, Chen Z. Critical review of the impact of tortuosity on diffusion. *Chem Eng Sci*. 2007;62(14):3748–3755.
54. Levenspiel O. *Chemical Reaction Engineering*, 3rd ed. New York: Wiley, 1999.
55. Civan F. Relating permeability to pore connectivity using a power-law flow unit equation. *Petrophysics*. 2002;43(06):457–476.
56. Civan F. Scale effect on porosity and permeability: kinetics, model, and correlation. *AIChE J*. 2001;47(2):271–287.
57. McCune CC, Fogler HS, Kline WE. An experimental technique for obtaining permeability-porosity relationships in acidized porous media. *Ind Eng Chem Fundam*. 1979;18(2):188–191.
58. Bird RB, Stewart WE, Lightfoot EN. *Transport Phenomena*, 2nd ed. New York: Wiley, 2002.
59. Civan F. Improved permeability equation from the bundle-of-leaky-capillary-tubes model. *SPE Production Operations Symposium,* Oklahoma City, OK, 2005.
60. Civan F. Leaky-tube permeability model for identification characterization and calibration of reservoir flow units. *SPE Annual Technical Conference and Exhibition,* Denver, CO, 2003.
61. Civan F. Fractal formulation of the porosity and permeability relationship resulting in a power-law flow units equation-a leaky-tube model. *International Symposium and Exhibition on Formation Damage Control,* Lafayette, LA, 2002.
62. Civan F. Predictability of porosity and permeability alterations by geochemical and geomechanical rock and fluid interactions. *SPE International Symposium on Formation Damage Control,* Lafayette, LA, 2000.
63. Civan F. Non-isothermal permeability impairment by fines migration and deposition in porous media including dispersive transport. *Transp Porous Media*. 2010;85(1):233–258.
64. Civan F. Applicability of the Vogel–Tammann–Fulcher type asymptotic exponential functions for ice, hydrates, and polystyrene latex. *J Colloid Interface Sci*. 2005;285(1):429–432.
65. Civan F. Discussion of a practical method for anticipating asphaltene problems. *SPE Prod Oper*. 2006;21(03):411–411.
66. Civan F. Temperature dependence of wettability related rock properties correlated by the Arrhenius equation. *Petrophysics*. 2004;45(4):350–362.
67. Nagy KD. *Catalyst Immobilization Techniques for Continuous Flow Synthesis*. Department of Chemical Engineering, Massachusetts Institute of Technology, Cambridge, MA, 2011.
68. Ramachandran V, Fogler HS. Plugging by hydrodynamic bridging during flow of stable colloidal particles within cylindrical pores. *J Fluid Mech*. 1999;385:129–156.

Manuscript received Mar. 1, 2014, and revision received June 16, 2014.